

A Neuroskeletal Atlas: Spatial Mapping and Contextualization of Axon Subtypes Innervating the Long Bones of C3H and B6 Mice

Madelyn R Lorenz,^{1†} Jennifer M Brazill,^{1†} Alec T Beeve,^{1,2‡} Ivana Shen,¹ and Erica L Scheller^{1,2} 

¹Division of Bone and Mineral Diseases, Department of Medicine, Washington University School of Medicine, St. Louis, MO, USA

²Department of Biomedical Engineering, Washington University, St. Louis, MO, USA

ABSTRACT

Nerves in bone play well-established roles in pain and vasoregulation and have been associated with progression of skeletal disorders, including osteoporosis, fracture, arthritis, and tumor metastasis. However, isolation of the region-specific mechanisms underlying these relationships is limited by our lack of quantitative methods for neuroskeletal analysis and precise maps of skeletal innervation. To overcome these limitations, we developed an optimized workflow for imaging and quantitative analysis of axons in and around the bone, including validation of Baf53b-Cre in concert with R26R-tdTomato (Ai9) as a robust pan-neuronal reporter system for use in musculoskeletal tissues. In addition, we created comprehensive maps of sympathetic adrenergic and sensory peptidergic axons within and around the full length of the femur and tibia in two strains of mice (B6 and C3H). In the periosteum, these maps were related to the surrounding musculature, including entheses and myotendinous attachments to bone. Three distinct patterns of periosteal innervation (termed type I, II, III) were defined at sites that are important for bone pain, bone repair, and skeletal homeostasis. For the first time, our results establish a gradient of bone marrow axon density that increases from proximal to distal along the length of the tibia and define key regions of interest for neuroskeletal studies. Lastly, this information was related to major nerve branches and local maps of specialized mechanoreceptors. This detailed mapping and contextualization of the axonal subtypes innervating the skeleton is intended to serve as a guide during the design, implementation, and interpretation of future neuroskeletal studies and was compiled as a resource for the field as part of the NIH SPARC consortium. © 2021 The Authors. *Journal of Bone and Mineral Research* published by Wiley Periodicals LLC on behalf of American Society for Bone and Mineral Research (ASBMR).

KEY WORDS: BONE-BRAIN-NERVOUS SYSTEM INTERACTIONS; BONE-FAT INTERACTIONS; BONE-MUSCLE INTERACTIONS

Introduction

Peripheral nerves target nearly every organ in the body to communicate afferent and efferent signals to and from the brain; the skeleton is no exception.⁽¹⁾ Neurons in and around the bone have well-established roles in the generation and maintenance of pain associated with skeletal pathologies, including fracture, tumor progression, and arthritis.^(2–4) Within cortical bone and bone marrow, sensory and sympathetic nerve fibers track with the arteriolar vasculature^(5–7) and coordinate vasoregulatory responses.^(8–11) Additional functions of skeletal axons have also been proposed, including modulation of bone formation and turnover in the context of skeletal development,⁽¹²⁾ adaptation

to mechanical loading,^(13,14) repair, and regeneration,^(15–17) as well as regulation of bone marrow adipocyte metabolism,⁽¹⁸⁾ joint disease,⁽¹⁹⁾ and control of hematopoietic cell maturation and egress.⁽²⁰⁾

Direct neural modulation of skeletal function is dependent upon the precise localization of axons near target cells and the capacity of the neurons to sense the bone microenvironment and/or to release neurotransmitters. The most well-characterized skeletal nerve fibers are sensory peptidergic axons, the majority of which are marked by calcitonin gene-related peptide (CGRP), and sympathetic adrenergic axons containing tyrosine hydroxylase (TH), the rate-limiting enzyme in catecholamine synthesis.⁽⁶⁾ These neuronal subtypes have been shown to innervate the

This is an open access article under the terms of the Creative Commons Attribution-NonCommercial License, which permits use, distribution and reproduction in any medium, provided the original work is properly cited and is not used for commercial purposes.

Received in original form September 30, 2020; revised form February 5, 2021; accepted February 11, 2021. Accepted manuscript online February 16, 2021.

Address correspondence to: Erica L Scheller, DDS, PhD, Washington University, 660 South Euclid Avenue, Campus Box 8301, St. Louis, MO 63110, USA.

E-mail: scheller@wustl.edu

Additional Supporting Information may be found in the online version of this article.

†MRL, JMB, and ATB contributed equally to this work.

Journal of Bone and Mineral Research, Vol. 36, No. 5, May 2021, pp 1012–1025.

DOI: 10.1002/jbmr.4273

© 2021 The Authors. *Journal of Bone and Mineral Research* published by Wiley Periodicals LLC on behalf of American Society for Bone and Mineral Research (ASBMR).

periosteum in a meshwork pattern, traverse the cortical bone through nutrient canals, and ramify within the marrow cavity.⁽⁶⁾ Skeletal axon varicosities, presumed sites of neurotransmitter release and receptor clustering, have been observed in close proximity to bony surfaces and resident osteoblasts, osteoclasts, and their precursors, as well as at sites of bone marrow adipose tissue and hematopoietic cells.^(21,22) Although the morphology and molecular phenotype of skeletal axons have been well studied,⁽²³⁾ the inherent challenges of visualizing and quantifying neural fibers in calcified tissue have led to a functional and anatomical neuroskeletal map that is incomplete. This is complicated by the heterogeneity of the bone architecture, the complex tissue interactions therein, and the opposing influences of the sensory and sympathetic arms of the nervous system that converge to influence the physiological functions of the skeleton.⁽¹⁾

To begin to overcome this, we used thick-section immunohistochemistry and tissue clearing, in concert with high-resolution imaging and axon quantification techniques, to comprehensively map skeletal axons within and around the femur and tibia. In addition, we used the Baf53b-Cre-R26R-tdTomato (Ai9) reporter system to corroborate the neural specificity of our immunolabeling and further identify a Baf53b+ axon subpopulation innervating the skeleton. Lastly, we defined the location, prevalence, and morphology of specialized mechanoreceptor endings. This information has been compiled into a reference atlas of skeletal innervation that can be used to inform future neuroskeletal studies. This resource was generated as part of the SPARC consortium (Stimulating Peripheral Activity to Relieve Conditions), a call by the National Institutes of Health in the United States to generate foundational neuroanatomic maps of axons within peripheral tissues with the aim of supporting the development of novel neuroceuticals for targeted treatment of pain and other conditions.

Materials and Methods

Key reagents and resources used in this study are detailed in Supplemental Table S1.

Mice

All work was performed as approved by the animal use and care committee at Washington University (St. Louis, MO, USA). Mice were housed on a 12-hour light/dark cycle and fed *ad libitum* (PicoLab 5053, LabDiet, St. Louis, MO, USA). C57BL6J (JAX Strain #000664), C3H/HeJ (JAX Strain #000659), Baf53b-Cre (JAX Strain #027826), and Ai9 reporter mice (JAX Strain #007909) were obtained from Jackson Laboratories (Bar Harbor, ME, USA). Schwann cell reporter mice were a kind gift of Dr Jeffrey Milbrandt and were generated by crossing the following strains: P₀-Cre (JAX Strain 017927)⁽²⁴⁾ and Ai9-flox/flox (JAX Strain 007909).⁽²⁵⁾

Histology and immunostaining

Tissue isolation and embedding

Mice were anesthetized with ketamine/xylazine and perfused through the left ventricle of the heart with 10 mL phosphate buffered saline followed by 10 mL 10% neutral buffered formalin (NBF; Thermo Fisher Scientific, Waltham, MA, USA; 23–245684). For all experiments, collected tissues were post-fixed in 10%

NBF for 24-hours. After fixation, tissues were washed for 2 hours in diH₂O. Bones were fully decalcified in 14% EDTA (Sigma-Aldrich, St. Louis, MO, USA; E5134), pH 7.4 and equilibrated in 30% sucrose solution before embedding in OCT mounting media (Fisher HealthCare 23–730-571, Thermo Fisher Scientific).

Antibody optimization and storage

CGRP, TH, and NF200 antibody dilutions were optimized using mixed neural and skeletal tissue (frozen sections through the spinal column containing vertebral bone, spinal cord, and dorsal root ganglion). Antibody dilutions were selected based on positive staining of target neural cells and axons with minimal background staining in surrounding tissues. Antibody use and storage are detailed in Supplemental Table S2.

Frozen immunostaining and imaging

Embedded tissues were cut at 50 μ m on a cryostat (Leica, Buffalo Grove, IL, USA). For immunostaining, cut sections on Colorfrost Plus glass slides (Thermo Fisher Scientific 12-550-18) were blocked in 10% donkey serum in TNT buffer before incubation for 48 hours with primary antibodies at 4°C (Supplemental Table S2). After washing 3 \times 5 minutes, secondary antibodies in TNT buffer were applied for 24 hours at 4°C (Supplemental Table S2). The sections were then washed 3 \times 5 minutes in TNT buffer, incubated in DAPI (Sigma-Aldrich) for 5 minutes, and washed again before mounting with Fluoromount-G (Thermo Fisher Scientific 00-4958-02). For Figs. 1–3, 5, and Supplemental Files A–D, serial tiled images were taken with a 10 \times objective on a Nikon (Tokyo, Japan) spinning disk confocal microscope (μ m/px = 0.650, step size = 2.5 μ m, number of steps = 21). Stitching of the nd2 multipoint files was done using the FIJI Stitching plugin “snake by rows.” For Fig. 5, serial tile images were obtained using a Leica confocal at 10 \times (μ m/px = 0.6968, step size = 2.5 μ m, number of steps = 41) with automatic stitching through the LASX Software. Step-by-step tissue preparation and immunostaining instructions are also available at protocols.io (DOI: dx.doi.org/10.17504/protocols.io.bqu2mwye).

Confocal image segmentation and analysis

Selection of quantification regions

From the longitudinal array of slides created for each bone, four sections were chosen corresponding to the metaphysis, mid-diaphysis with tibial ridge, diaphysis proximal to the TFJ, and diaphysis just distal to the TFJ. For each of the above regions, sections were chosen based on morphological similarity, including bone shape and attachment sites.

Generation of tissue masks

A combined cancellous and cortical bone mask was generated simultaneously by thresholding max projections of the FITC channel (green) in FIJI.⁽²⁶⁾ Optimal upper and lower thresholds were chosen to remove muscle, connective tissue, marrow, and other background cellularity (some speckle and small holes in bone were allowed at this stage). After thresholding, bone masks were manually corrected based on the source file in ImageJ by clearing non-bone elements using the freehand selection tool. A median filter (radius = 11) was applied to smooth the mask. Medullary masks were generated by inverting the bone mask in FIJI, drawing a circle inside the cortical ring using the freehand selection tool, and clearing outside the selection. Cancellous and cortical bone

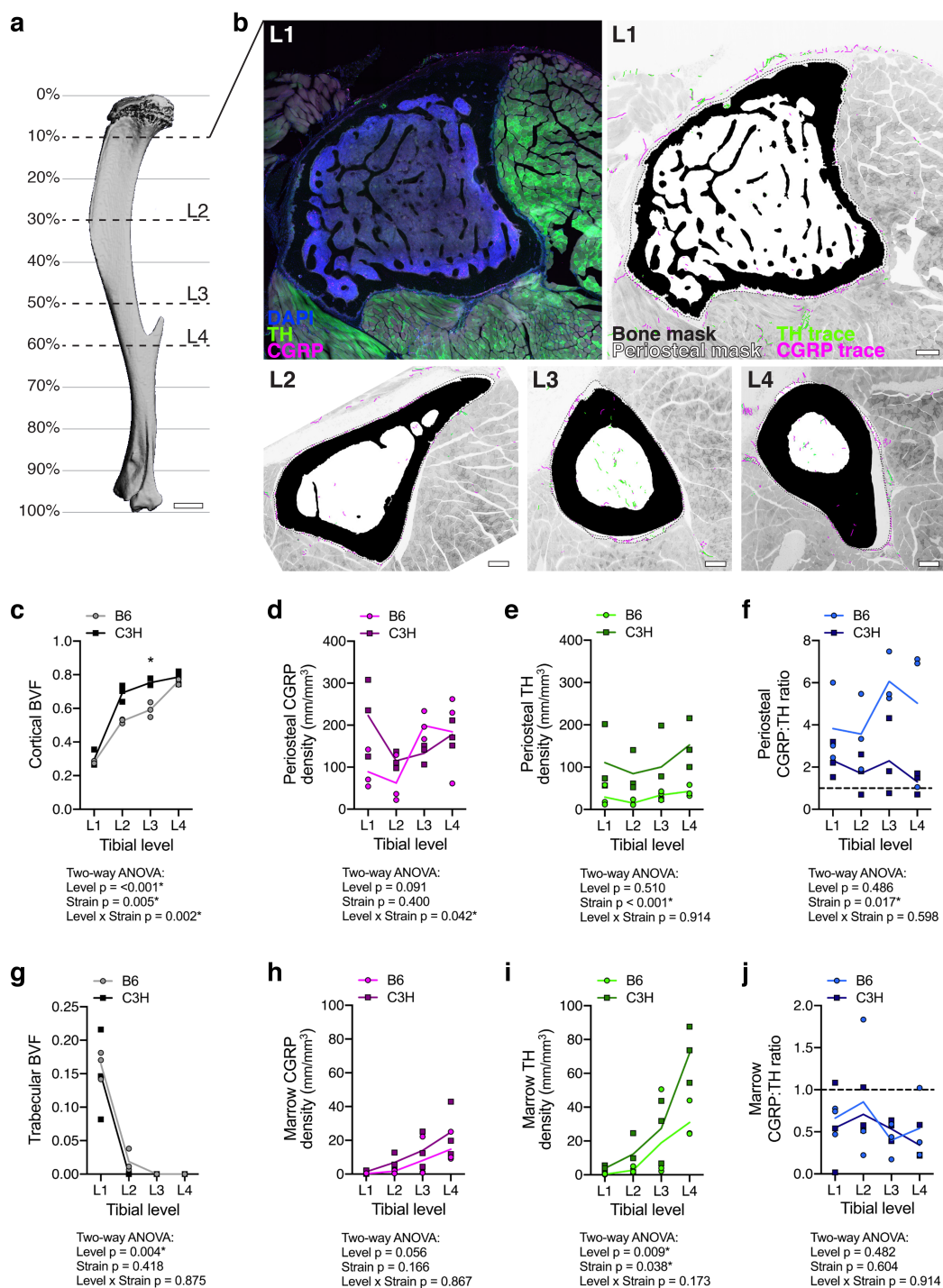


Fig 1. Neuroskeletal axon density varies by bone compartment, tibial level, and mouse strain. (A) 3D rendering of a μ CT scan of a 12-week-old male B6 tibia, lateral view. L₁ to L₄ represent levels analyzed as distinguished by cross-sectional bone morphology. Percentages demarcate approximate distance from the knee as a percentage of total tibia length. Scale bar = 1 mm. (B) L₁ left: representative confocal micrograph through a 50- μ m-thick transverse cross section with immunolabeled CGRP+ sensory axons (magenta) and TH+ sympathetic axons (green), as well as DAPI+ nuclei (blue). L₁ right and L₂ to L₄: bone mask (black), periosteal mask (dotted line), CGRP+ axon traces (magenta), and TH+ axon traces (green) overlaid on a grayscale max projection to visualize tibial innervation in the context of the musculoskeletal system at the metaphysis (L₁), the diaphysis with tibial ridge (L₂), and the diaphysis proximal to the TFJ (L₃) and distal to the TFJ (L₄). Scale bars = 200 μ m. (C–J) Quantification of compartmentalized bone volume fraction (BVF) and innervation density from B6 and C3H mice at each level represented A and B. (C) BVF of cortical bone. (D, E) CGRP+ and TH+ axon density (mm/mm³) within the overlying periosteum. (F) Periosteal CGRP:TH ratio. (G) BVF of trabecular bone. (H, I) CGRP+ and TH+ axon density (mm/mm³) within the marrow cavity. (J) Marrow CGRP:TH ratio. Data points represent individual animals with a mean trendline; $n = 3$ for each strain and level; two-way ANOVA with Sidak's multiple comparisons test; $*p < .050$.

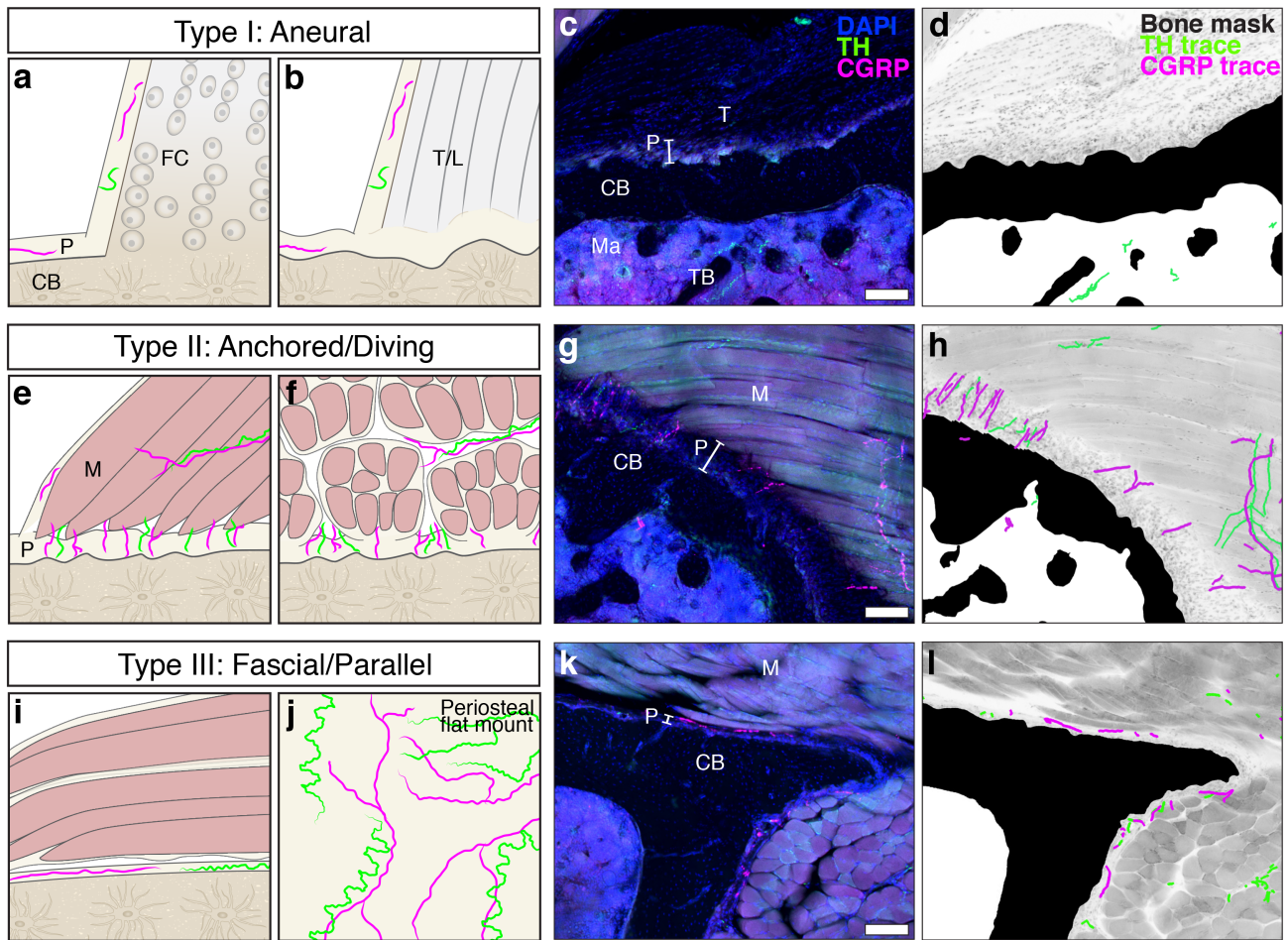


Fig 2. Peripheral axons innervate the periosteum in three distinct patterns (type I, II, III). (A–D) Type I: aneural patterns are found at entheses, sites where tendons or ligaments attach to the cortical bone (CB) surface. Aneural regions of the periosteum are devoid of CGRP+ (magenta) and TH+ (green) axons. (A) Tendinous fibers connect seamlessly to bone through unmineralized and mineralized fibrocartilage tissue (FC) at fibrocartilaginous entheses. (B) The tendon or ligament (T/L) is continuous with a thick fibrous layer of the periosteum (P) at fibrous entheses. (C) Confocal micrograph through a 50-µm-thick transverse cross section of a tibia from a 12-week-old C3H male with immunolabeled CGRP+ sensory axons (magenta) and TH+ sympathetic axons (green), as well as DAPI+ nuclei. (D) Corresponding neuroskeletal traced/masked analysis overlaid on a grayscale max projection demonstrating an aneural enthesis at the tibia metaphysis where the semimembranosus tendon (T) attaches to the bone. Trabecular bone (TB) is visible in the marrow cavity (ma). (E–H) Type II: anchored/diving innervation patterns are found at sites where axons transit directly from the associated muscle (M) tissue through the fibrous and cambium layers of the periosteum at a 90-degree angle to the cortical bone surface as visualized here in the C3H tibia where the popliteus muscle attaches to the bone. (I–L) Type III: fascial/parallel innervation patterns are found at sites where fascia attach to bone. Axons are woven through the thin periosteal layer at these sites and run parallel to the bone surface as evident in cross section (I, K, L). The mesh-like network of periosteal axons at these sites is clearly visualized by periosteal whole-mount preparation (J; see Martin et al.⁽⁷⁾ and Thai et al.⁽⁴⁰⁾). Scale bars = 100 µm.

masks were produced using the medullary mask, clearing inside or outside the marrow cavity. Lastly, holes in the cancellous and cortical bone masks were filled using the FIJI binary operation Fill Holes. In cases where cortical bone completely enclosed the marrow cavity, a small path was cleared from the cortex before performing the binary operation and was subsequently repaired.

The periosteum was defined as a thin, densely cellular layer adjacent to cortical bone. Based on the max projections of the FITC channel in FIJI, upper and lower thresholds were chosen to segment the periosteum. Using previous masks, the bone and marrow were deleted from the periosteal mask. Masks were manually corrected in ImageJ using the freehand selection tool. The DAPI channel was frequently referenced to differentiate periosteum from other connective tissues and fascia. A median filter (radius = 6) was applied to

smooth the mask, and lastly holes in the periosteum were filled using the FIJI binary operation Fill Holes to create a continuous layer. In cases where the periosteum made a complete ring, a small path was cleared from the periosteum before performing the binary operation and was subsequently repaired.

Cortical and cancellous BV/TV calculation

The area of the cortical bone, cancellous bone, and marrow cavity were calculated in FIJI from the masks created by thresholding-based segmentation described above. Cortical BV/TV was calculated as cortical bone area/(cortical bone area + marrow area), and cancellous BV/TV was calculated as cancellous bone area/marrow area.

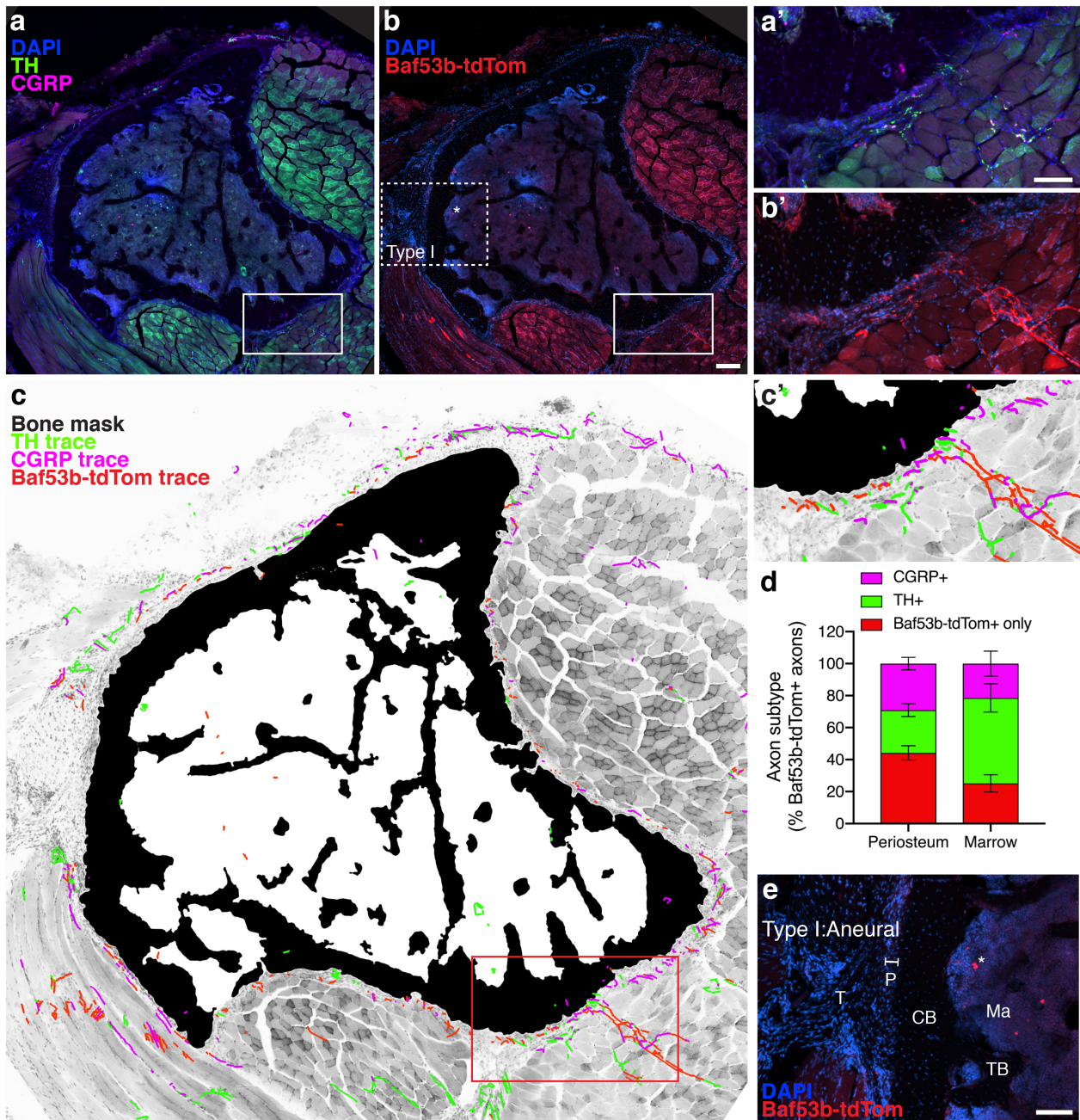


Fig 3. Baf53b-tdTomato is a robust, selective reporter system for skeletal innervation. (A, B) Representative confocal micrograph of a proximal tibial cross section with immunolabeled CGRP+ sensory axons (magenta) and TH+ sympathetic axons (green) with DAPI+ nuclei (blue, A), and tdTomato expression driven by Baf53b-Cre, as well as DAPI+ nuclei (blue, B). Asterisks indicate non-neural, autofluorescence. Scale bar = 200 μ m. (C) Bone mask (black), CGRP+ axon traces (magenta), TH+ axon traces (green), and Baf53b-tdTomato + axon traces overlaid on a grayscale max projection to visualize tibial innervation. CGRP+ and TH+ axons were also positive for Baf53b-tdTomato. (A'–C') High magnification of the periosteal innervation of the solid boxed region indicated in A–C. Scale bar = 100 μ m. (D) Quantification of compartmentalized axonal subtypes pooled from L₁ to L₄ represented as a percentage of total Baf53b-tdTomato + axons. Bars represent mean with SEM; *n* = 3 individual animals quantified at each level. (E) Aneural region of the periosteum (P), where tendon (T) connects to cortical bone (CB), is devoid of Baf53b-tdTomato+ axons. TB = trabecular bone; ma = marrow. Scale bar = 100 μ m.

Axon tracing and quantification

TH+, CGRP+, and Baf53b-tdTomato+ axons were independently traced with the Simple Neurite Tracer plugin⁽²⁷⁾ to obtain total axon length. The volume of the periosteum and marrow cavity were calculated as the area multiplied by a section thickness of

50 μ m. Volumetric density of fiber lengths was calculated as the total length of fibers traced divided by the corresponding volume for the region traced. Identification of nerves within the bone marrow is more challenging than at other sites because of non-specific autofluorescence, poor light penetration, and the presence of antibody-dependent cellular staining. This can result

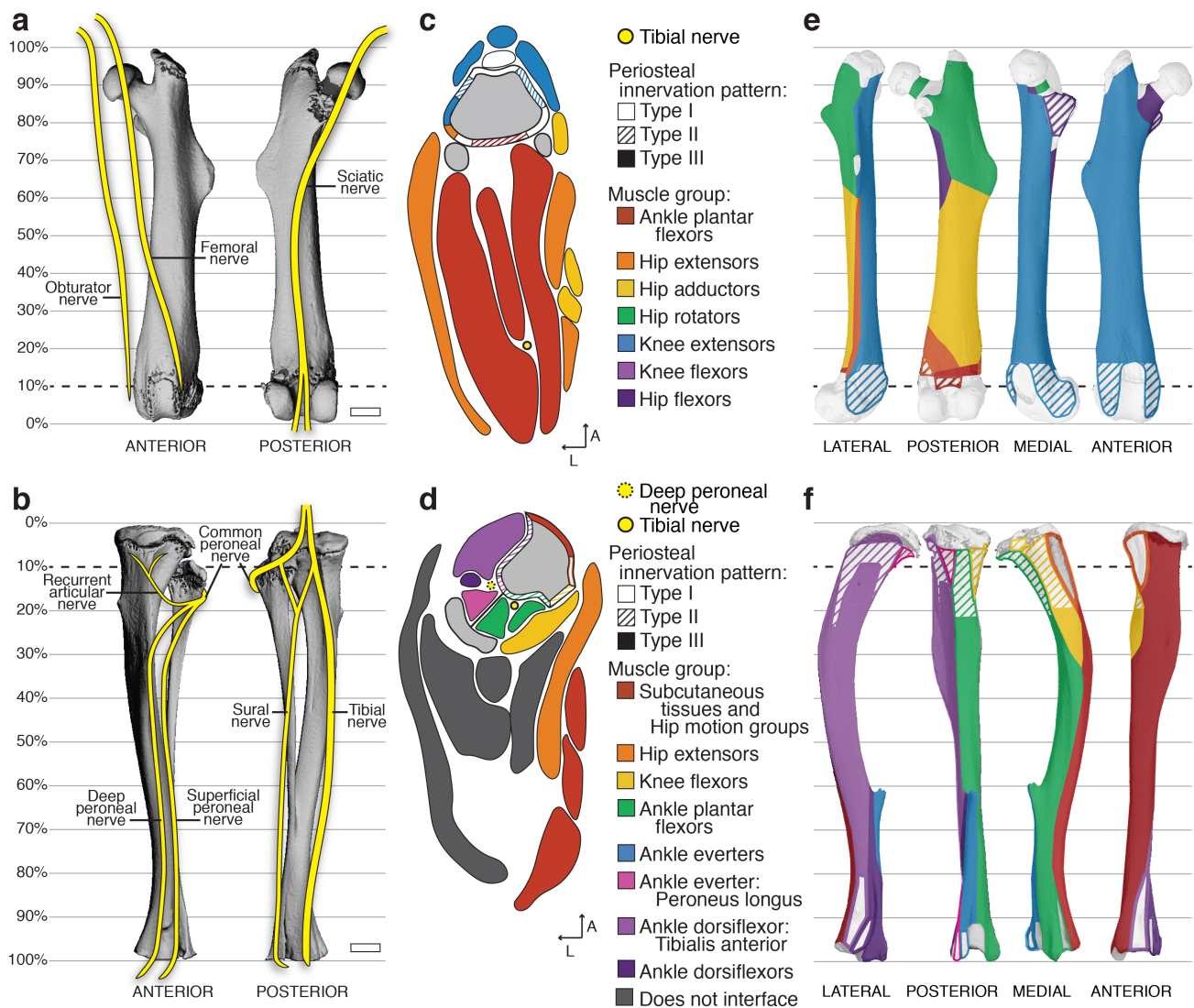


Fig 4. Relationships between peripheral nerves and periosteal axon patterns and the musculoskeletal system. (A, B) Schematic of major nerve branches in the anterior and posterior thigh (A) and leg (B) overlaid on 3D-rendered- μ CT scans of the left femur and tibia-fibula, respectively. Scale bars = 1 mm. (C, D) Representative 2D maps of transverse cross sections through (C) the thigh at the level of 10% of the total femur length proximal to the knee and (D) the leg at 10% of the total tibial length distal to the knee. The bone is indicated in gray and the superimposed periosteal innervation patterns are distinguished by pattern-fill and are color-coded to the interfacing muscle group indicated by the key. Detailed maps including labels of individual muscles are available in the atlases (Supplemental Files A–D). (E, F) Three-dimensional periosteal innervation maps overlaid on the lateral, posterior, medial, and anterior aspects of the μ CT-rendered (E) femur and (F) tibia.

in staining artifacts, as noted with an information icon (“i”) when they appear in the atlas (Supplemental Files A–D). Strategies to overcome these limitations include technical optimization, tissue clearing, tiled confocal images of thick frozen sections to capture large-volume data sets, and strict morphologic criteria for nerve selection.

Axon tracing image overlays

Axon tracings were exported from the Simple Neurite Tracer plugin in FIJI. This exported file preserves the coordinates of the traced axons and assigns each traced segment a line with a width of one pixel. Exported nerve masks were dilated four times using the binary processing tool, increasing the width of each

traced axon to 9 pixels for the purposes of visualization. After this, bone and nerve masks were imported into Adobe Photoshop and overlaid on a grayscale max projection of the FITC and DAPI channels from the original image. This results in a visually accurate map of axon length, branching, orientation, and relative density. However, features such as absolute nerve diameter are not preserved.

Micro-CT and maps

Representative two- and three-dimensional maps of the type I, II, and III periosteal innervation patterns were generated after comprehensive review of serial images generated every 150 μ m

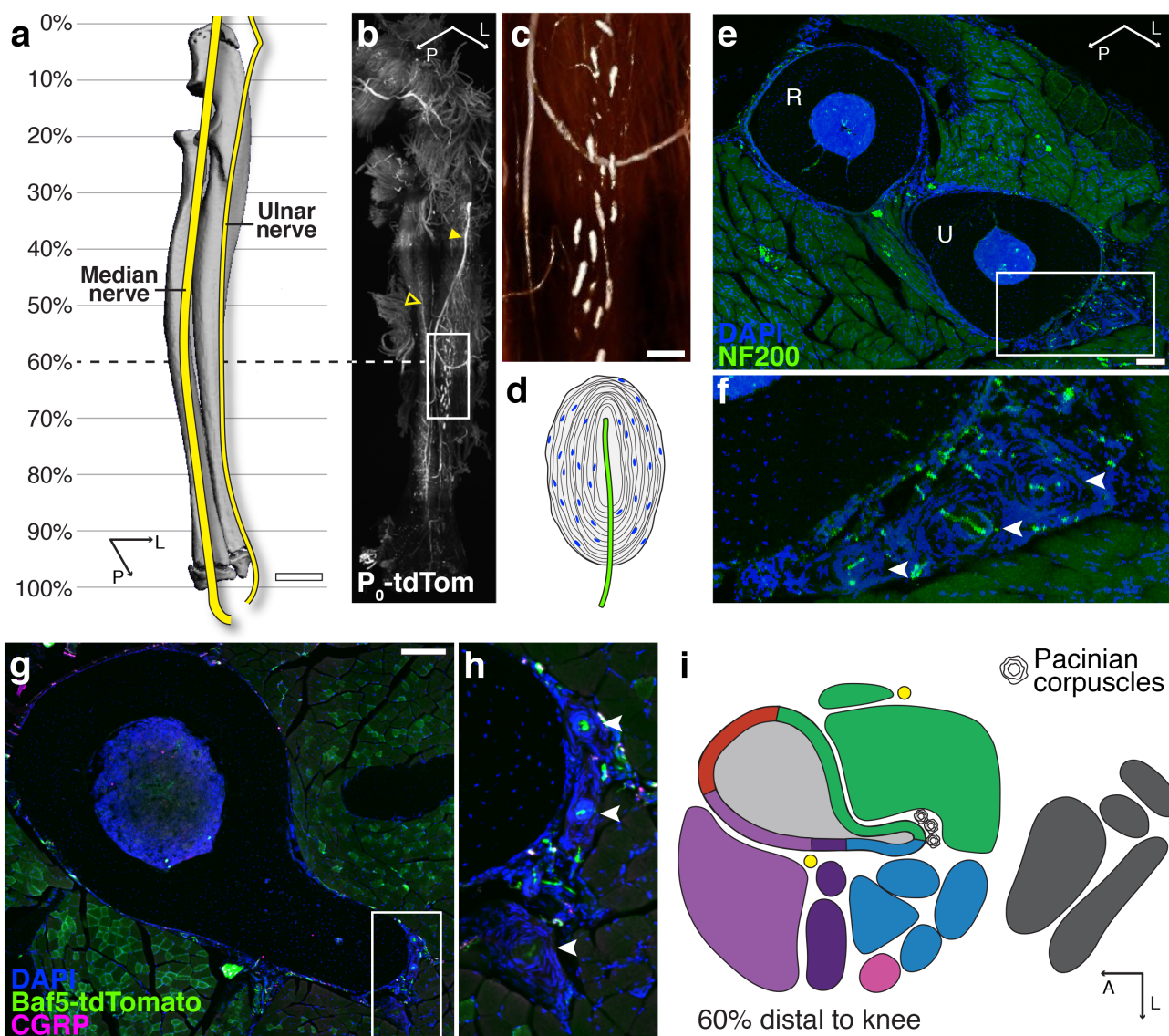


Fig 5. Specialized mechanoreceptor endings are associated with the skeleton of the forearm and lower leg. (A) Schematic of major nerve branches in the forearm overlaid on a 3D-rendered μ CT scan of the radius–ulna. Scale bar = 1 mm. (B) Light-sheet image of a cleared forearm from an adult Schwann cell reporter mouse (P_0 -tdTomato) revealing the ulnar nerve (filled arrowhead) and median nerve (empty arrowhead) and the distribution of Pacinian corpuscles on the ulnar surface. (C) High-magnification, intensity-pseudocolored image of the boxed region in B. Scale bar = 200 μ m. (D) Drawing of a Pacinian corpuscle demonstrating the lamellar structure derived from Schwann cells surrounding a single unmyelinated ending of a large, myelinated sensory axon. (E) Representative confocal micrograph through a 100- μ m-thick transverse cross section through the radius (R) and ulna (U) and surrounding musculature visualized by DAPI (blue) and NF200 (green) immunolabeling at 60% of the ulnar length. Scale bar = 200 μ m. (F) High magnification of the corpuscles (arrowheads) on the lateral aspect of the ulna of the boxed region indicated in E. (G) Representative confocal projection of a 50- μ m-thick transverse cross section of a tibia from a Baf53b-tdTomato (green) reporter mouse with immunolabeling CGRP+ axons (magenta) along with DAPI staining (blue) at 60% of the tibial length distal to the knee. Scale bar = 200 μ m. (H) High magnification of the Pacinian corpuscles on the posterior aspect of the tibia of the boxed region indicated in G. (I) 2D map corresponding to the confocal image in G indicating the location of Pacinian corpuscles found in all strains and sexes at this level of the tibia. Additional information can be found in the supplemental tibial atlases (Supplemental Files C, D).

along the length of the femur and tibia from four independent mice (12-week-old B6 male, B6 female, C3H male, C3H female). A representative 3D model, color-coded to match surrounding functional muscle groups, was then reconstructed in Adobe Photoshop using scans of the tibias of 12-week-old B6 and C3H male mice performed on a Scanco μ CT 40 (Scanco Medical AG, Bassersdorf, Switzerland; 55 kVp, 145 μ A, 300 ms integration time, 16 μ m voxel size). 2D schematics showing muscle

attachments and muscle labeling were generated in Adobe Illustrator. These were adapted from Charles and colleagues⁽²⁸⁾ with muscle placement and innervation patterns adjusted based on our serial section analysis. Type I, II, and III innervation patterns were illustrated on the bone-tissue interface in the 2D schematics and color-coded in relation to surrounding muscle attachments and fascial structures. The final atlas was compiled with Adobe InDesign.

Whole-mount tissue clearing and imaging

Tissue clearing was performed as previously described with minor modification.⁽²⁹⁾ Briefly, mice were intracardially perfused with 20 mL 0.02 M PBS followed by 20 mL of fresh 4% paraformaldehyde. Immediately after perfusion, dissected tissues were post-fixed in 4% PFA at 4°C overnight. The post-fixed limb was then incubated in A4P0 hydrogel overnight (5 mL 40% acrylamide, 45 mL of PBS, and 0.125 g of VA044) and polymerized at 38°C for 6 hours. The forelimb was then incubated in 8% SDS at 37°C for 5 days to fully clear muscle and bone tissue. After 2 days of thorough PBS washing, the forelimb was incubated in 25% quadrol at 37°C for 2 days. After another 2 days of thorough washing in PBS, the bones were incubated in 1.42 and 1.48 RIMS of Histodenz for 1 day each before imaging. Images were taken with 4× objective on the SmartSPIM imaging system through the full length of the bone and 3D reconstructed with ORS (Montreal, Canada) Dragonfly Software for visualization of the P₀+ Schwann cells.

Statistics

Statistical analyses were performed in GraphPad (La Jolla, CA, USA) Prism. Specific tests are indicated in the figure legends. A *p* value <.05 was considered statistically significant.

Results

Validation of neuroskeletal immunoassay and axon quantification in the C3H and B6 mouse tibia

Before creating the atlas, we validated our axon tracing and immunostaining paradigm relative to previous publications (Table 1).^(6,30,31) To achieve this, we quantified CGRP+ peptidergic sensory and TH+ adrenergic sympathetic axons in the periosteum and bone marrow of 12-week-old male C57BL/6J (B6) and C3H/HeJ mice (C3H) at four levels along the length of the tibia. Region-specific bone parameters including cortical and trabecular bone volume fraction (BVF) were also assessed. Levels of the tibia selected for analysis were distinguished by bone morphology at the metaphysis, mid-diaphysis with tibial ridge, the diaphysis proximal to the tibia-fibula junction (TFJ), and the diaphysis just distal to the TFJ. Analyzed levels approximated to 10% (L₁), 30% (L₂), 50% (L₃), and 60% (L₄) distal to the knee for B6 mice (Fig. 1A, B). Consistent with previous reports,^(32,33) the diaphyseal cortical BVF was significantly higher in C3H than B6 mice (L₂, L₃; Fig. 1C). However, cortical BVF was matched in the two strains at both the proximal and distal metaphysis (L₁, L₄; Fig. 1C). Trabecular BVF was comparable in both strains at the proximal metaphysis (L₁; Fig. 1G), also consistent with prior comparisons at this region and age.⁽³⁴⁾ Trabecular bone was largely absent in the tibial diaphysis of both B6 and C3H mice (L₂ to L₄).

At each level, CGRP+ sensory and TH+ sympathetic axons were traced, and the total fiber length within each compartment was expressed relative to the total compartment volume (Fig. 1B). As reported previously for femur (Table 1), the periosteum was the most densely innervated compartment of the tibia for both B6 and C3H mice. Within the periosteum, we found that CGRP+ sensory axons demonstrated level-specific densities that were dependent on mouse strain (Fig. 1D). By contrast, TH+ sympathetic axon density was relatively constant along the length of the periosteum. C3H mice had a greater absolute TH+ fiber density at all levels relative to B6 (Fig. 1E). Independent of strain,

periosteal CGRP+ sensory fibers were more prevalent than TH+ sympathetics at all levels of the tibia (periosteal CGRP:TH ratio > 1; Fig. 1F). This ratio was higher in B6 animals than C3H (Fig. 1F). Within the marrow cavity, innervation density increased from proximal to distal independent of strain (Fig. 1H, I). Converse to the ratio of neural subtypes observed in the periosteum, TH+ sympathetic innervation consistently exceeded CGRP+ sensory innervation in all regions of the bone marrow (CGRP:TH ratio < 1; Fig. 1J). Overall, our immunolabeling and analysis paradigm corroborates previous reports of compartmentalized innervation density (Table 1), and additionally demonstrates that this varies by strain. Our results further establish a gradient of bone marrow axon density that increases from proximal to distal along the length of the tibia.

Identification of three distinct patterns of periosteal innervation (type I, II, III)

Next, we applied this validated CGRP and TH immunolabeling and tracing paradigm to assess the periosteal axon profiles throughout the entire length and circumference of the tibia and femur of male and female 12-week-old C3H and B6 mice. The periosteum is the layer of connective tissue that envelops the bone and provides a supportive microenvironment for vasculature, nerves, and periosteal cells.^(35,36) We identified three consistent patterns of adult periosteal innervation that aligned with both the attachments formed between the periosteum and the surrounding tissues and the orientation of the nerve axons, independent of mouse sex or strain. Within each innervation pattern, we observed variations in local axon density and orientation that should be considered for future studies pertaining to the relationships between nerves and bone, as described below.

Type I: aneural

Many regions of the bone surface were aneural, completely lacking CGRP+ sensory or TH+ sympathetic innervation (Fig. 2A–D). Aneural regions were observed primarily where tendons or ligaments interfaced with the bone at sites called entheses. There are two main classes of entheses: fibrocartilaginous and fibrous.^(37,38) Fibrocartilaginous entheses comprise continuous zones connecting tendinous fibers through unmineralized and mineralized fibrocartilage tissue that blend imperceptibly into bone (Fig. 2A). At fibrous entheses, the tendon is continuous with a thick fibrous layer of the periosteum (Fig. 2B). The only axons found in these regions were located in the fascial tissue lining the tendon or ligament, often referred to as the epitenon. Type I regions greatly contributed to the discontinuous nature of periosteal innervation.

Type II: anchored/diving

In other regions, axons transited directly from the associated muscle tissue through the fibrous and cambium layers of the periosteum at a 90-degree angle to the cortical bone surface (Fig. 2E–H). Type II regions contained TH+ sympathetic axons and an abundance of CGRP+ sensory axons that appeared to dive from the sarcolemma or muscle fascia to the bone surface. Regions with a diving innervation pattern aligned most closely with sites where muscle is connected to periosteal bone by partially mineralized fiber anchors, known also as extrinsic fibers or Sharpey's fibers.⁽³⁹⁾

Table 1. Previous Quantification of TH+ and CGRP+ Axon Density in Mouse Bone

Publication	Mouse information	Bone	Compartment	Immunostain	Summary of validated results
Mach et al., 2002 ⁽⁶⁾	C3H/HeJ male 6–7 weeks, 20–25 g	Femur proximal head, diaphysis, distal head	Periosteum, cortical bone, bone marrow	CGRP TH	<ul style="list-style-type: none"> • Nerve density: periosteum > bone marrow • In periosteum, CGRP > TH (1.3- to 2.4-fold) • In bone marrow, CGRP < TH (0.3- to 0.5-fold)
Castañeda-Corral et al., 2011 ⁽³⁰⁾	C3H/HeJ male 20–25 g	Distal femur	Periosteum, cortical bone, bone marrow	CGRP	<ul style="list-style-type: none"> • Nerve density: periosteum > bone marrow • TH not assessed
Chartier et al., 2018 ⁽³¹⁾	C57Bl/6J male 10 days, 3 months, 24 months	Distal femur	Periosteum, bone marrow, cortical pores	CGRP TH	<ul style="list-style-type: none"> • Nerve density: periosteum > bone marrow • 3-month periosteum CGRP > TH (1.3-fold) • 3-month bone marrow CGRP < TH (0.7-fold)

Type III: fascial/parallel

The most prevalent pattern of innervation observed consisted of a meshwork of CGRP+ sensory and TH+ sympathetic axons within the periosteum where fascia attached to the bone (Fig. 2I–L). At these sites, the periosteal layer is relatively thin and the axons run close to the bone, parallel to the cortical surface. This type III meshwork pattern is apparent in periosteal whole-mount preparations taken from regions of the bone where the absence of tendinous or extrinsic fibers allows for separation of the periosteum from adjacent tissues (Fig. 2J).^(7,30,40)

Application of the selective, pan-neuronal reporter system Baf53b-tdTomato in the skeleton

The Baf53b-Cre transgenic mouse line was previously reported to exhibit Cre expression in neurons of the central and peripheral nervous system but not in progenitors, glia, and most non-neural cells.⁽⁴¹⁾ In this study, we crossed Baf53b-Cre mice with reporter mice containing a floxed R26R-tdTomato (Ai9) allele⁽²⁵⁾ to examine the utility of this reporter system for quantification and visualization of nerves in and around the bone (referred to here as Baf53b-tdTomato). Transverse sections of the tibia were costained with TH and CGRP to further validate the sensitivity and specificity of our immunostaining protocol. We found robust, neural-specific expression of Baf53b-tdTomato throughout the musculoskeletal system (Fig. 3A–C). Leveraging our imaging and axon tracing paradigm in these tibial sections further corroborated the neural origin and specificity of our TH and CGRP immunolabeling, as TH+ or CGRP+ axons localized with the axonal Baf53b-tdTomato signal (Fig. 3A–C). The density of each of these peripheral axon subpopulations was quantified as a percent of the total axons within the periosteum and bone marrow. We identified nerve fibers in both bone compartments that were positive only for Baf53b-tdTomato (mean ± SD; 44.2% ± 14.8 in the periosteum and 25.1% ± 18.0 in the bone marrow; Fig. 3D), revealing a significant proportion of skeletal axons that do not express CGRP or TH. This Baf53b-tdTomato-only population appears to include entire axons originating from distinct neural subpopulations and intermittent segments of CGRP+ and TH+ axons that do not contain immunostained neurotransmitter or enzyme. Lastly, we evaluated the Baf53b + axon phenotype and orientation within the type I, II, and III periosteal

regions (Fig. 2). This revealed that differential axon profiles were maintained in type II and type III regions and further confirmed that regions of the bone surface identified as type I were aneural (Fig. 3E).

Generation of 2D and 3D maps of type I–III periosteal innervation patterns in relation to overlying nerves and muscles

Nerve supply of the limb

Axons innervating the femur are primarily derived from the femoral nerve (Fig. 4A). The femoral nerve runs along the anteromedial aspect of the femur and provides innervation to the muscle groups that function as knee extensors (rectus femoris and vastus muscles).^(42,43) It also provides the innervation to the anterior and medial aspects of the femur bone.^(44,45) The obturator nerve runs nearby, also anteromedial to the femur, and innervates the hip adductors (gracilis anterior, gracilis posterior, adductor longus, adductor magnus) and some hip rotators in the gluteal region (quadratus femoris, obturator externus). There is no current evidence that the obturator nerve innervates the femur bone. The sciatic nerve runs along the posterior aspect of the femur and innervates the posterior femoral muscles that function as hip extensors (semitendinosus, semimembranosus, caudofemoralis, biceps femoris).^(42,43) A segment of the posterior femur bone is also innervated by the sciatic nerve.⁽⁴⁶⁾

Slightly above the posterior aspect of the knee, the sciatic nerve branches into the tibial and common peroneal nerves. Innervation of the tibia bone is primarily derived from the sciatic nerve (Fig. 4B) with evidence in humans for minor sensory contributions by the terminal branches of the femoral nerve in the medial regions of the proximal tibial epiphysis/metaphysis and distal epiphysis.^(44,46) The tibial branch of the sciatic nerve runs down the leg on the posterior side of the tibia with the peroneal artery and veins and innervates the knee flexors, ankle plantar flexors, hip extensors, and hip motion groups in addition to the tibia bone.^(42,43) By contrast, the common peroneal nerve wraps around the fibula to the front of the tibia. It sends a branch termed the recurrent articular nerve to the region of the proximal epiphysis and joint. Distally, it splits into the superficial peroneal nerve and the deep peroneal nerve. The deep peroneal nerve runs between the tibia and fibula along the interosseous

membrane and, in addition to innervating the tibia bone, it sends smaller branches that innervate muscles of the ankle everter and dorsiflexor families, including the tibialis anterior.^(42,43)

Two-dimensional muscle maps with type I–III innervation patterns

The periosteum is a fascial connective tissue that is continuous with other layers of limb fascia including the epitenon and epimysium. To facilitate the consideration of periosteal axon patterns within the context of these boundaries, we created representative schematics showing muscle attachments and muscle labeling (Fig. 4C, D). These were adapted from Charles and colleagues⁽²⁸⁾ with muscle placement and innervation patterns adjusted based on our serial immunostaining analysis. Type I, II, and III innervation patterns were illustrated on the bone-tissue interface in the cross-sectional schematics and color-coded in relation to surrounding muscle attachments. This process was repeated along the length of the femur and tibia, as presented in the atlas compilation (Supplemental Files A–D) and overview section in Fig. 4.

Three-dimensional type I–III innervation pattern maps

In addition to the 2D maps, the localization of each periosteal innervation pattern was mapped onto the surface of the femur and tibia and color-coded to match surrounding muscle groups (Fig. 4E, F). Type I aneural regions were localized to the epiphyses and metaphyses of the tibia and femur. Type II anchored/diving regions were primarily localized in the metaphyses and along the diaphyses of the long bones. There were noted differences in the prevalence of type II regions between B6 and C3H bones; these can be explored in more detail in the atlases (Supplemental Files A–D). Type III fascial/parallel innervation was prominent on bone surfaces interfaced with loosely adherent fascia, such as with extra-skeletal adipose tissue, epitenon, and unanchored areas of the epimysium. A type III pattern was also found on the intraosseous fascial membranes between connected long bones, such as the tibia and fibula.

Mapping of specialized mechanoreceptor endings

The skeleton is primarily innervated by neurons with small, finely myelinated and/or unmyelinated axons.⁽²³⁾ However, in specific regions, large-diameter axons with specialized mechanoreceptor endings known as Pacinian corpuscles have also been identified in association with the interosseous membranes and the periosteum of large mammals.^(47,48) This has not been clearly demonstrated or mapped in the mouse. To overcome this, we generated reporter mice with a floxed R26R-tdTomato (Ai9) allele expressing Cre recombinase under control of the *myelin protein zero* (*P₀*) gene promoter to label mature myelinating Schwann cells and their precursors (referred to as *P₀*-tdTomato).⁽²⁴⁾ Schwann cells are the main glial cells of the peripheral nervous system. In addition to labeling myelinated axons, we found that the *P₀*-tdTomato reporter system labels the lamellar Schwann cell layers that make up the outer structure of the Pacinian corpuscle. Whole-bone tissue clearing and light-sheet microscopy of the forearm of the *P₀*-tdTomato reporter mouse revealed major nerve branches and the distribution of Pacinian corpuscles along the lateral aspect of the ulna 50% to 70% distal to the elbow (Fig. 5A–C). In cross sections, Pacinian corpuscles could be identified morphologically as a single myelinated sensory fiber (NF200+) in the center of a lamellar capsule that was closely approximated to, though not continuous with, the

periosteum (Fig. 5D–F). Central axons were also positive for Baf53b and negative for CGRP and TH (Fig. 5G, H). Serial cross-section examination of Pacinian corpuscles in the limb localized these specialized mechanoreceptors exclusively to the mid-diaphyseal and distal regions of the tibia (Fig. 5G–I) as mapped in the atlases (Supplemental Files C, D).

Limb atlases—overview and contents

These observations and outcomes were compiled into four interactive atlases that cover the prevalence, localization, and morphology of the CGRP+ sensory and TH+ sympathetic nerve fibers in and around the femur (Supplemental Files A, B) and tibia (Supplemental Files C, D), in addition to their relationship with the overlying musculature, fascial tissue, and perilipin-positive bone marrow and extraskelatal adipocytes. Unique cross sections were selected from serial analysis, annotated by relative distance to the knee joint. The longitudinal range of the bone that comprises similar bone morphology, as well as continuous periosteal innervation patterns and common tissue interfaces is indicated on each page to facilitate sectioning of regions of interest. Additional features and proposed use of these atlases are detailed in Fig. 6.

Discussion

The innervation of the skeleton is not uniform. In this article, we demonstrate that peripheral axon subtype-specific densities and morphology vary by bone compartment and site and are influenced by mouse genetic strain. This dynamic, region-specific innervation of the bone and bone marrow likely influences pain and cellular function in states of skeletal homeostasis and in targeted areas of bone injury and inflammation. The maps provided here are intended to serve as a baseline reference and guide during the design and selection of regions of interest for future neuroskeletal studies in the femur, tibia, and beyond. For example, though not mapped in detail, our light-sheet imaging suggests that the nerve patterns and localization of specialized mechanoreceptors within the forelimb, another common site used for skeletal research, mimic those detailed in the tibia. In addition, the tissue preparation, immunostaining, imaging, and nerve quantification methods reported here may be easily applied in any control or transgenic mouse model of targeted injury, pharmacologic intervention, or systemic disease.

Previous mapping studies in the femur (Table 1) demonstrate that the periosteum is the most densely innervated compartment, where CGRP+ peptidergic sensory axons predominate, whereas TH+ sympathetic axons are more prevalent in the marrow cavity. For the first time, we corroborate these findings in the tibia, and additionally identify a strain-independent proximal-to-distal increase in bone marrow axon density. We anticipate that these findings reflect a primarily arterial localization of sympathetic axons; a vast intra-marrow sinusoidal network runs the length of the tibia, with a proximal-to-distal increase in arterial density.⁽⁴⁹⁾ We also report that the periosteum and marrow of B6 mice are overall less densely innervated by sympathetic axons compared with C3H mice. Although the functional significance of these observations remains to be clarified, the localized density of specific axonal subtypes has distinct functional implications. Neural contributions to adaptive loading, as well as fracture pain and healing, have been largely ascribed to local sensory fibers in the periosteum.^(17,50,51) Neural contributions to hematopoiesis and skeletal metastasis have been attributed

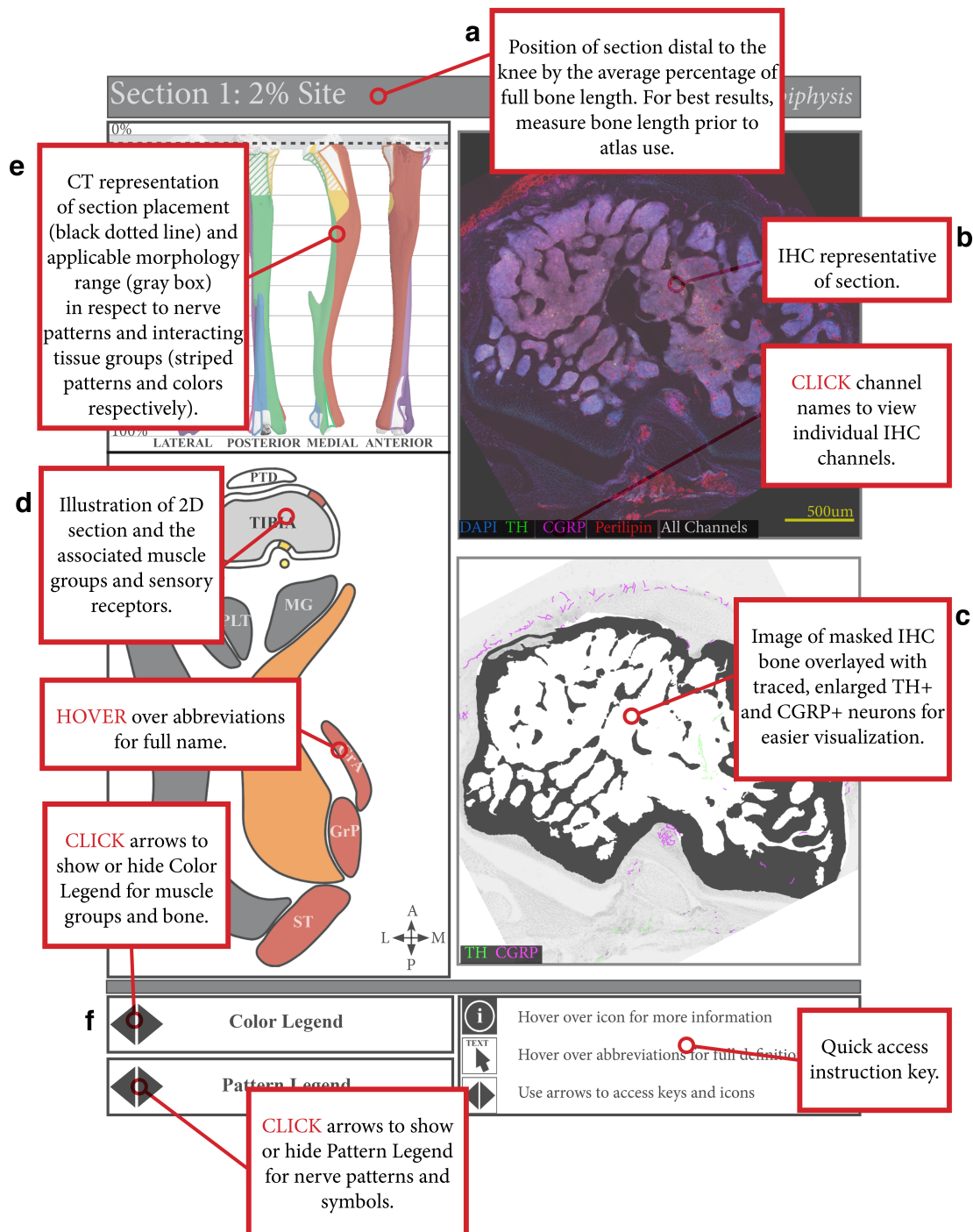


Fig 6. Mouse limb atlases—guide for use. (A) The four supplemental atlases comprise systematic analyses of serial, transverse cross sections down the length of the femur and tibia in B6 and C3H mice, where each page details a section of the bone at a particular percent distance from the knee. This includes (B) representative confocal projections of immunohistochemically labeled CGRP+ sensory and TH+ sympathetic nerve fibers, along with perilipin+ adipocytes and DAPI-stained nuclei, in and around the bone and (C) corresponding bone-masked, axon-traced overlays to highlight and visualize the neuroskeletal features. (D) In addition, the atlas contains 2D reference maps with pattern-coded periosteal innervation patterns superimposed on the bone interface and related to color-coded muscle groups and individual muscle identities. (E) Lastly, these 2D maps served as the basis for 3D mapping of periosteal innervation patterns and color-coded muscle groups onto the lateral, posterior, medial, and anterior aspects of the corresponding bone. (F) Instructions for accessing interactive features are located at the bottom of the page, such as displaying innervation pattern legend, muscle group color legend, and full muscle identifiers, or toggling through confocal channels.

to sympathetic activity,^(52,53) in line with the intimate association of sympathetic fibers with the arteriolar vasculature and their relative abundance in the marrow. Both arms of the peripheral nervous system have been implicated in skeletal homeostasis, suggesting counter-regulatory mechanisms afforded by sensory and sympathetic innervation coexist to maintain bone homeostasis, for example, by coordinating opposing effects on vascular tone or osteoblast function.⁽¹⁾ Additionally, our work with the Baf53b-tdTomato reporter system suggests that CGRP+ peptidergic sensory axons and TH+ sympathetic adrenergic axons account for at least 20% to 30% and 25% to 50%, respectively, of the total nerve population innervating the skeleton. Non-peptidergic sensory axons and sympathetic cholinergic axons have been reported to target the skeleton^(23,40,54,55) but have not been reliably marked and mapped. Identifying the full complement of neural subpopulations that innervate the bone represents an important area of future investigation to understand the physiological role of neuroskeletal interactions.

Another key question that needs to be addressed by future work is the localization and prevalence of signaling sites that allow nerves to communicate with skeletal target cells or to sense target tissue signals. True synapses have not been found in bone, consistent with non-synaptic neurotransmitter release from sympathetic and small/medium sensory fibers in more thoroughly characterized peripheral target tissues such as skin and smooth muscles of the intestine and arterioles.⁽⁵⁶⁾ Instead, vesicular release of neurotransmitters likely occurs *en passage* at axon varicosities devoid of myelin. This means that vesicular neurotransmitter release, in addition to other nerve-mediated signaling events, can occur along the length of the axon in addition to at the end. These putative release sites have been previously identified along the length of the distal axons in the vicinity of skeletal target cells by ultrastructural analysis by our lab as well as others.^(21,22,57–59) In the future, super-high-resolution immunofluorescent imaging of presynaptic markers in combination with ultrastructural analysis of vesicle-rich, myelin-free varicosities will be required to definitively assess neurotransmitter release sites along the length of skeletal axons, similar to what has been achieved for sympathetic neuroeffector junctions on arrector pili muscles attached to the hair follicle.⁽⁶⁰⁾ Although this type of work is beyond the scope of the current study, it is our intention that the map of skeletal axons provided here serves as a guide to examine sites of neuroskeletal communication in more targeted regions of interest in future studies.

As detailed throughout the atlases, bone is intimately associated with the nervous, vascular, and muscular systems. Particularly exciting potential exists in overlaying this neuroskeletal map with whole-bone maps of load-induced strain and adaptation,⁽⁶¹⁾ vascularity,⁽⁴⁹⁾ and stem-cell distribution^(62,63) to elucidate more defined functional roles of skeletal axons. Periosteal axon patterning, which we have characterized and defined as type I–III, is aligned to connections of muscle and fascia to the bone. Strain maps could be related to periosteal innervation patterns to give insight to their functional role in load-induced adaptation; type II anchored/diving axons may integrate muscle cues to the loaded bone, while axons in type III fascial/parallel regions might amplify bone formation on surfaces that lack large connective tissue strain. The endocortical surface, by contrast, is relatively aneural and likely derives its regulation primarily from the underlying osteocyte network in addition to the adjacent bone marrow and stromal compartment. Axonal orientation is less defined in the bone marrow, but TH+ fibers generally cluster around central arterioles, whereas CGRP+ axons are more

disperse (Supplemental Files A–D). The non-overlapping sensory and sympathetic axons within the bone marrow may be suggestive of spatially defined mechanisms regulating unique progenitor cell pools.^(18,20) The axonal patterning in the periosteum and bone marrow was largely conserved in the mice characterized in this study, irrespective of sex or strain. Additionally, this work highlights the need to consider the role of Schwann cells in the bidirectional cross-talk between nerves and bone. Schwann cells not only insulate axons but can also initiate and modulate neural signaling, as well as contribute to tissue repair,^(64–66) and remain an underexplored component of the neuroskeletal system.

As we move forward, it is clear that a systematic and comprehensive map of skeletal innervation related to region-specific bone surfaces and bone marrow compartments is fundamental to assigning physiologic functions to local neuronal populations. In addition, the neuroskeletal field needs standardized nomenclature to facilitate more comprehensive and cohesive studies. In this resource, we have provided protocols and easy-to-apply methods for axon visualization and quantification. Quantifying the length and density of skeletal axons using semi-automated tracing with Simple Neurite Tracer⁽²⁷⁾ can overcome non-uniform localization of the labeled molecules and inherent differences in staining and fluorophore signal-to-noise ratios for comparative studies. Based on our analysis of the Baf53b-tdTomato reporter, neuroskeletal quantification using axon-localized neurotransmitters and enzymes is accurate when strict morphologic criteria are applied but may underestimate the true length of the axons when the immunotarget is intermittent. When possible, we recommend the use of genetically encoded reporter systems such as Baf53b-tdTomato for tracking and mapping of skeletal axons. At present, two-dimensional quantification is somewhat limited by orientation of the axon to the plane of the section, but this methodology can be extrapolated to 3D analysis when lightsheet microscopy and high-computational power are more accessible. In addition, we have presented four interactive atlases that can be applied as a reference during study design, implementation, and interpretation. Lastly, based on this work, we propose that future studies report several basic metrics to help to unify the field. Specifically, (i) section orientation (transverse, longitudinal), (ii) the analyzed level along the length of the bone (eg, 40% from the knee), (iii) the bone surface (eg, anterior tibial ridge), and (iv) the axon pattern(s) analyzed (eg, types II and/or III). This will help to ensure reproducibility between studies while moving the field toward development of new therapies for treatment of musculoskeletal pain and disease.

Disclosures

All authors state that they have no conflicts of interest.

Acknowledgments

This work was supported by grants from the National Institutes of Health, including U01-DK116317 (ELS) and T32-AR060719 (JMB, ATB). We are thankful to the Musculoskeletal Research Center (MRC, P30-AR074992) and the Washington University Center for Cellular Imaging (WUCCI), with particular thanks to James Fitzpatrick and Peter Bayguinov, for their support. In addition, we thank Jeff Stirman at SmartSPIM for generating the lightsheet image used in this publication.

Data availability: All relevant data are available from the authors upon reasonable request. The curated B6 and C3H

reference atlases are provided here as Supplemental Files A, B (femur) and Supplemental Files C, D (tibia). The raw confocal images used for the generation of the reference atlases is available as a curated data set in collaboration with the NIH SPARC consortium and Blackfyinn data repository (data set DOI: 10.26275/ztgw-jz3r).

Author contributions: MRL: Conceptualization; data curation; investigation; methodology; software; validation; visualization; writing-original draft; writing-review & editing. JMB: Conceptualization; data curation; investigation; methodology; software; validation; visualization; writing-original draft; writing-review & editing. ATB: Conceptualization; data curation; formal analysis; investigation; methodology; software; validation; visualization; writing-original draft; writing-review & editing. IS: Formal analysis; investigation; writing-review & editing. ELS: Conceptualization; data curation; formal analysis; funding acquisition; investigation; methodology; project administration; resources; software; supervision; validation; visualization; writing-original draft; writing-review & editing.

PEER REVIEW

The peer review history for this article is available at <https://publons.com/publon/10.1002/jbmr.4273>.

References

1. Brazill JM, Beeve AT, Craft CS, Ivanusic JJ, Scheller EL. Nerves in bone: evolving concepts in pain and anabolism. *J Bone Miner Res.* 2019;34(8):1393-1406.
2. O'Neill TW, Felson DT. Mechanisms of osteoarthritis (OA) pain. *Curr Osteoporos Rep.* 2018;16(5):611-616.
3. Ivanusic JJ. Molecular mechanisms that contribute to bone marrow pain. *Front Neurol.* 2017;8:458.
4. Mantyh PW. The neurobiology of skeletal pain. *Eur J Neurosci.* 2014;39(3):508-519.
5. Sayilekshmy M, Hansen RB, Delaissé J-M, Rolighed L, Andersen TL, Heegaard A-M. Innervation is higher above bone remodeling surfaces and in cortical pores in human bone: lessons from patients with primary hyperparathyroidism. *Sci Rep.* 2019;9(1):5361.
6. Mach DB, Rogers SD, Sabino MC, et al. Origins of skeletal pain: sensory and sympathetic innervation of the mouse femur. *Neuroscience.* 2002;113(1):155-166.
7. Martin CD, Jimenez-Andrade JM, Ghilardi JR, Mantyh PW. Organization of a unique net-like meshwork of CGRP+ sensory fibers in the mouse periosteum: implications for the generation and maintenance of bone fracture pain. *Neurosci Lett.* 2007;427(3):148-152.
8. Fukuta H, Mitsui R, Takano H, Hashitani H. Contractile properties of periosteal arterioles in the Guinea-pig tibia. *Pflugers Arch.* 2017;469(9):1203-1213.
9. Fukuta H, Mitsui R, Takano H, Hashitani H. Neural regulation of the contractility of nutrient artery in the Guinea pig tibia. *Pflugers Arch.* 2020;472(4):481-494.
10. Wee NKY, Lorenz MR, Bekirov Y, Jacquin MF, Scheller EL. Shared autonomic pathways connect bone marrow and peripheral adipose tissues across the central neuraxis. *Front Endocrinol.* 2019;10:668.
11. Ferrell WR, Khoshbaten A, Angerson WJ. Responses of bone and joint blood vessels in cats and rabbits to electrical stimulation of nerves supplying the knee. *J Physiol.* 1990;431:677-687.
12. Tomlinson RE, Li Z, Zhang Q, et al. NGF-TrkA signaling by sensory nerves coordinates the vascularization and ossification of developing endochondral Bone. *Cell Rep.* 2016;16(10):2723-2735.
13. Heffner MA, Genetos DC, Christiansen BA. Bone adaptation to mechanical loading in a mouse model of reduced peripheral sensory nerve function. *PLoS One.* 2017;12(10):e0187354.
14. Sample SJ, Behan M, Smith L, et al. Functional adaptation to loading of a single bone is neuronally regulated and involves multiple bones. *J Bone Miner Res.* 2008;23(9):1372-1381.
15. Madsen JE, Hukkanen M, Aune AK, et al. Fracture healing and callus innervation after peripheral nerve resection in rats. *Clin Orthop.* 1998;351:230-240.
16. Zhang Y, Xu J, Ruan YC, et al. Implant-derived magnesium induces local neuronal production of CGRP to improve bone-fracture healing in rats. *Nat Med.* 2016;22(10):1160-1169.
17. Chartier SR, Thompson ML, Longo G, Fealk MN, Majuta LA, Mantyh PW. Exuberant sprouting of sensory and sympathetic nerve fibers in nonhealed bone fractures and the generation and maintenance of chronic skeletal pain. *Pain.* 2014;155(11):2323-2336.
18. Hu B, Lv X, Chen H, et al. Sensory nerves regulate mesenchymal stromal cell lineage commitment by tuning sympathetic tones. *J Clin Invest.* 2020;130(7):3483-3498.
19. Zhu S, Zhu J, Zhen G, et al. Subchondral bone osteoclasts induce sensory innervation and osteoarthritis pain. *J Clin Invest.* 2019;129(3):1076-1093.
20. Katayama Y, Battista M, Kao W-M, et al. Signals from the sympathetic nervous system regulate hematopoietic stem cell egress from bone marrow. *Cell.* 2006;124(2):407-421.
21. Robles H, Park S, Joens MS, Fitzpatrick JAJ, Craft CS, Scheller EL. Characterization of the bone marrow adipocyte niche with three-dimensional electron microscopy. *Bone.* 2018;118:89-98.
22. Imai S, Tokunaga Y, Maeda T, Kikkawa M, Hukuda S. Calcitonin gene-related peptide, substance P, and tyrosine hydroxylase-immunoreactive innervation of rat bone marrows: an immunohistochemical and ultrastructural investigation on possible efferent and afferent mechanisms. *J Orthop Res.* 1997;15(1):133-140.
23. Ivanusic JJ. Size, neurochemistry, and segmental distribution of sensory neurons innervating the rat tibia. *J Comp Neurol.* 2009;517(3):276-283.
24. Feltri ML, D'Antonio M, Previtali S, Fasolini M, Messing A, Wrabetz L. PO-Cre transgenic mice for inactivation of adhesion molecules in Schwann cells. *Ann N Y Acad Sci.* 1999;883:116-123.
25. Madisen L, Zwingman TA, Sunkin SM, et al. A robust and high-throughput Cre reporting and characterization system for the whole mouse brain. *Nat Neurosci.* 2010;13(1):133-140.
26. Schindelin J, Arganda-Carreras I, Frise E, et al. Fiji: an open-source platform for biological-image analysis. *Nat Methods.* 2012;9(7):676-682.
27. Longair MH, Baker DA, Armstrong JD. Simple Neurite Tracer: open source software for reconstruction, visualization and analysis of neuronal processes. *Bioinformatics.* 2011;27(17):2453-2454.
28. Charles JP, Cappellari O, Spence AJ, Hutchinson JR, Wells DJ. Musculoskeletal geometry, muscle architecture and functional specializations of the mouse hindlimb. *PLoS One.* 2016;11(4):e0147669.
29. Greenbaum A, Chan KY, Dobreva T, et al. Bone CLARITY: clearing, imaging, and computational analysis of osteoprogenitors within intact bone marrow. *Sci Transl Med.* 2017;9(387):eaah6518.
30. Castañeda-Corral G, Jimenez-Andrade JM, Bloom AP, et al. The majority of myelinated and unmyelinated sensory nerve fibers that innervate bone express the tropomyosin receptor kinase a. *Neuroscience.* 2011;178:196-207.
31. Chartier SR, Mitchell SAT, Majuta LA, Mantyh PW. The changing sensory and sympathetic innervation of the young, adult and aging mouse femur. *Neuroscience.* 2018;387:178-190.
32. Judex S, Garman R, Squire M, Donahue L-R, Rubin C. Genetically based influences on the site-specific regulation of trabecular and cortical bone morphology. *J Bone Miner Res.* 2004;19(4):600-606.
33. Beamer WG, Donahue LR, Rosen CJ, Baylink DJ. Genetic variability in adult bone density among inbred strains of mice. *Bone.* 1996;18(5):397-403.
34. Scheller EL, Doucette CR, Learman BS, et al. Region-specific variation in the properties of skeletal adipocytes reveals regulated and constitutive marrow adipose tissues. *Nat Commun.* 2015;6(1):7808.
35. Orwoll ES. Toward an expanded understanding of the role of the periosteum in skeletal health. *J Bone Miner Res.* 2003;18(6):949-954.

36. Duchamp de Lageneste O, Julien A, Abou-Khalil R, et al. Periosteum contains skeletal stem cells with high bone regenerative potential controlled by Periostin. *Nat Commun.* 2018;9(1):773.
37. Apostolakis J, Durant TJ, Dwyer CR, et al. The enthesis: a review of the tendon-to-bone insertion. *Muscles Ligaments Tendons J.* 2014;4(3):333-342.
38. Suzuki D, Murakami G, Minoura N. Histology of the bone-tendon interfaces of limb muscles in lizards. *Ann Anat.* 2002;184(4):363-377.
39. Aaron JE. Periosteal Sharpey's fibers: a novel bone matrix regulatory system? *Front Endocrinol.* 2012;3:98.
40. Thai J, Kyloh M, Travis L, Spencer NJ, Ivanusic JJ. Identifying spinal afferent (sensory) nerve endings that innervate the marrow cavity and periosteum using anterograde tracing. *J Comp Neurol.* 2020;528(11):1903-1916.
41. Zhan X, Cao M, Yoo AS, et al. Generation of BAF53b-Cre transgenic mice with pan-neuronal Cre activities. *Genes.* 2015;53(7):440-448.
42. Greene EC. *Anatomy of the rat.* New York, NY: Hafner Pub. Co.; 1955.
43. Waxman SG. *Clinical neuroanatomy.* 27th ed. New York, NY: McGraw-Hill Education/Medical; 2013.
44. NYSORA. Ultrasound-guided femoral nerve block [Internet]. 2018. Available at: <https://www.nysora.com/techniques/lower-extremity/ultrasound-guided-femoral-nerve-block/>. Accessed 2020 Sep 13.
45. Mutty CE, Jensen EJ, Manka MA, Anders MJ, Bone LB. Femoral nerve block for diaphyseal and distal femoral fractures in the emergency department. Surgical technique. *J Bone Joint Surg Am.* 2008;90 (Suppl 2 Pt 2):218-226.
46. NYSORA. Ultrasound-guided sciatic nerve block [Internet]. 2018. Available at: <https://www.nysora.com/regional-anesthesia-for-specific-surgical-procedures/lower-extremity-regional-anesthesia-for-specific-surgical-procedures/foot-and-ankle/ultrasound-guided-sciatic-nerve-block-2/>. Accessed 2020 Sep 13.
47. Ferrington DG, Rowe MJ, Tarvin RP. Actions of single sensory fibres on cat dorsal column nuclei neurones: vibratory signalling in a one-to-one linkage. *J Physiol.* 1987;386:293-309.
48. Zelená J. Survival of Pacinian corpuscles after denervation in adult rats. *Cell Tissue Res.* 1982;224(3):673-683.
49. Grüneboom A, Hawwari I, Weidner D, et al. A network of trans-cortical capillaries as mainstay for blood circulation in long bones. *Nat Metab.* 2019;1(2):236-250.
50. Li Z, Meyers CA, Chang L, et al. Fracture repair requires TrkA signaling by skeletal sensory nerves. *J Clin Invest.* 2019;129(12):5137-5150.
51. Tomlinson RE, Li Z, Li Z. NGF-TrkA signaling in sensory nerves is required for skeletal adaptation to mechanical loads in mice. *Proc Natl Acad Sci U S A.* 2017;114(18):E3632-E3641.
52. Maryanovich M, Zahalka AH, Pierce H, et al. Adrenergic nerve degeneration in bone marrow drives aging of the hematopoietic stem cell niche. *Nat Med.* 2018;24(6):782-791.
53. Clément-Demange L, Mulcrone PL, Tabarestani TQ, Sterling JA, Eleftheriou F. β 2ARs stimulation in osteoblasts promotes breast cancer cell adhesion to bone marrow endothelial cells in an IL-1 β and selectin-dependent manner. *J Bone Oncol.* 2018;13:1-10.
54. Hohmann EL, Elde RP, Rysavy JA, Einzig S, Gebhard RL. Innervation of periosteum and bone by sympathetic vasoactive intestinal peptide-containing nerve fibers. *Science.* 1986;232(4752):868-871.
55. Jimenez-Andrade JM, Mantyh WG, Bloom AP, et al. A phenotypically restricted set of primary afferent nerve fibers innervate the bone versus skin: therapeutic opportunity for treating skeletal pain. *Bone.* 2010;46(2):306-313.
56. Burnstock G. Non-synaptic transmission at autonomic neuroeffector junctions. *Neurochem Int.* 2008;52(1-2):14-25.
57. Hara-Irie F, Amizuka N, Ozawa H. Immunohistochemical and ultrastructural localization of CGRP-positive nerve fibers at the epiphyseal trabeculae facing the growth plate of rat femurs. *Bone.* 1996;18(1):29-39.
58. Serre CM, Farlay D, Delmas PD, Chenu C. Evidence for a dense and intimate innervation of the bone tissue, including glutamate-containing fibers. *Bone.* 1999;25(6):623-629.
59. Takeda S, Eleftheriou F, Levasseur R, et al. Leptin regulates bone formation via the sympathetic nervous system. *Cell.* 2002;111(3):305-317.
60. Shwartz Y, Gonzalez-Celeiro M, Chen C-L, et al. Cell types promoting Goosebumps form a niche to regulate hair follicle stem cells. *Cell.* 2020;182(3):578-593.e19.
61. Carriero A, Pereira AF, Wilson AJ, et al. Spatial relationship between bone formation and mechanical stimulus within cortical bone: combining 3D fluorochrome mapping and poroelastic finite element modelling. *Bone Rep.* 2018;8:72-80.
62. Acar M, Kocherlakota KS, Murphy MM, et al. Deep imaging of bone marrow shows non-dividing stem cells are mainly perisinusoidal. *Nature.* 2015;526(7571):126-130.
63. Kokkaliaris K, Kunz L, Cabezas-Wallscheid N, et al. Adult blood stem cell localization reflects the abundance of reported bone marrow niche cell types and their combinations. *Blood.* 2020;136(20):2296-2307.
64. Yamazaki S, Ema H, Karlsson G, et al. Nonmyelinating Schwann cells maintain hematopoietic stem cell hibernation in the bone marrow niche. *Cell.* 2011;147(5):1146-1158.
65. Stierli S, Imperatore V, Lloyd AC. Schwann cell plasticity-roles in tissue homeostasis, regeneration, and disease. *Glia.* 2019;67(11):2203-2215.
66. Abdo H, Calvo-Enrique L, Lopez JM, et al. Specialized cutaneous Schwann cells initiate pain sensation. *Science.* 2019;365(6454):695-699.